Journal of Manufacturing Processes 80 (2022) 480–490

Contents lists available at ScienceDirect

Journal of Manufacturing Processes

journal homepage: www.elsevier.com/locate/manpro

Influence of surface roughness on the transient interfacial phenomena in laser impact welding

Glenn Gleason, Karl Bailey, Sumair Sunny, Arif Malik *, Rodrigo A. Bernal

Department of Mechanical Engineering, The University of Texas at Dallas, Richardson, TX 75080, USA

ARTICLE INFO

Keywords:
Laser impact welding
White light interferometry
Computational modeling
Surface roughness
Small-scale joining

ABSTRACT

Presented is an investigation into laser impact welding (LIW) wherein experimentally measured surface profiles of the flyer and target foils are incorporated to study their effects on the transient physical phenomena that occur during this rapid, collision-based joining process. During LIW, thermal response, plastic strains, and shear stresses evolve over a sub-microsecond timescale, which necessitates the use of computational modeling to predict the influence that surface roughness has on the material response and resulting joint morphology. White light interferometry is used to experimentally characterize the surface profiles of an aluminum 1100 flyer foil and a stainless steel 304 target foil. The profiles are mapped to material volumes within a plane strain, thermo-mechanical simulation employing an Eulerian framework. A spatially and temporally varying laser-induced plasma pressure is applied to the flyer foil, and the resulting transient phenomena are analyzed at timeframes ranging from initial contact through complete weld formation. To reveal effects of the rough foil surfaces, results from the same computational model using smooth foil surfaces are also obtained. When the rough surface profiles are included, it is found that significant differences in the thermal response and plastic strains are observed, and these differences are hypothesized to arise from the effects of discontinuous surface contact along the collision path. The incorporation of rough surface asperities also reveals two distinct regions prior to the weld initiation point; the first where elastic rebound occurs at a negligible collision angle, leaving interfacial voids, and the second where superficial shear deformation flattens the surfaces without mutual ablation and jetting. The work represents the first study in which measured surface profiles of the flyer and target foils are incorporated into a computational model of laser impact welding.

1. Introduction

Impact welding encompasses a wide range of largely solid-state joining processes involving a collision between two surfaces occurring at high relative velocities and at a particular range of contact angles, which results in mutual surface ablation and a bond with comparable strength to the parent materials [1,2]. Impact welding offers versatility in joining metallic components fabricated from alloys of differing thermomechanical properties (e.g., melting temperature), thus avoiding the formation of brittle intermetallic compounds, porosities, or micro cracks that often compromise weld quality between dissimilar materials when using fusion methods [3,4]. Additionally, the process has been shown capable of forming joints between immiscible metallic materials, such as magnesium and steel alloys [5].

Various impact welding methods have been developed for joining metallic parts of different scales and geometric configurations, and such methods are generally categorized according to their means of flyer propulsion, which can include the use of pressurized gases, explosives, magnetic discharge, or vaporizing foils [1,6]. This work focuses on laser impact welding (LIW) of thin metallic foils (~10 to 100 μm thickness) having potential applications in microelectronic or biomedical devices due to the uniquely small scale of the process [7,8]. Fig. 1 shows a schematic of LIW, with key phenomena and components labeled. The process begins with the short exposure of an absorptive ablative layer to a high-energy laser beam of short pulse duration (~17 ns in this work), which creates a highly pressurized plasma between the upper surface of the flyer foil and the confining layer (Fig. 1 *Left*). The expansion of the plasma causes the flyer to accelerate across a stand-off gap and collide at high velocity against the target foil. When the impact angle is within a certain range, material from the contacting surfaces is removed and "jetted" due to the action of concentrated, transient shear stresses. A springback region (Fig. 1 *Right*) may result due to insufficient impact

* Corresponding author.
E-mail address: Arif.Malik@utdallas.edu (A. Malik).

https://doi.org/10.1016/j.jmapro.2022.06.022
Received 12 February 2022; Received in revised form 3 June 2022; Accepted 13 June 2022
Available online 20 June 2022

angle at the weld center, resulting in a final weld that is annular in shape; Fig. 1 (*Inset*) shows a micrograph of an experimentally obtained LIW from an earlier publication by the authors [9].

Despite the use of impact welding in limited industrial applications [1], some issues remain in motivating its further adoption, such as finding methods to predictably induce the necessary weld front instability at specific locations so as to ensure desired final weld geometry. Impact welds form at a collision point between angled surfaces that travels near the speed of sound in the materials. This creates extreme pressures, plastic deformation, shear stresses, and temperature rises local to the forming interface; the resulting mutual ablation between the surfaces causes the formation of a jet, a necessary condition for continuous contact between uncontaminated substrates that creates a weld [11,12]. Moreover, when plastic strain rates exceed certain magnitudes ($\sim 10^6$ s^{-1} or higher), the material strengths appear to have negligible effects on the overall character of the process [13]. Indeed, analogies can be drawn between the behaviors near the advancing collision weld interfaces to that of fluid flow [14], and a description of the conditions at the forming joint may be summarized with a Reynolds number [15]. With the use of this analogy comes the characterization of the morphology of impact welds as being analogous to laminar flows (flat interfaces) and unstable flows (wavy interfaces with possible vortex shedding) [16–18]. Hence, realization of successful impact welding, including LIW, requires both the acceleration of a flyer to high velocity as well as the initiation of an interfacial instability, yet the latter in particular poses challenges for ensuring process reliability. Thus, there has been an increasing research attention on improving the quality and repeatability of impact welding, mainly through optimization of process parameters such as approach velocity of the surfaces, collision angle, collision point velocity, flyer thickness, and target thickness [2,19–22]. However, research that addresses the introduction of engineered surface features or the inherent roughness profiles to disturb the motion of the collision point, and thus establish greater control over the extent and character of welds, has been less prevalent. Nonetheless, drawing on stress-wave theories of impact welding, early work by Godunov et al. [23] as well as Szecket & Mayseless [24] (ref. Table 1) experimented with ledge features and embedded strips in target plates to trigger a steady-state, wavy interface that is analogous to introducing obstacles into transitional fluid flows. Work by Date et al. [25] and Bellmann et al. [12] investigated the relationship between the collision surfaces' roughness and the quality of the resulting joint, noting improved weld continuity between surfaces with lower average roughness values.

A review of the related work listed in Table 1 motivates further investigation into the LIW process with regard to effects of surface irregularities on weld quality. Note that in explosive welding (EXW) or kinetic impact welding methods, the ratio of the thickness of a flyer to the contact surfaces' average roughness, R_a, are 10^3 or greater, assuming typical R_a of 1 μm or less. In LIW experiments, however, flyer foils typically range in thickness from 30 to 50 μm [26,27], which is much closer to the order of magnitude of surface roughness, making it a more significant process design consideration. An investigation into roughness effects would establish the potential benefit in manufacturing LIW surfaces to be either as smooth as possible, or to have certain preferential surface characteristics. LIW may also be used for connections where mechanical joint strength is not the primary consideration, in favor, for example, of establishing corrosion protection wherein roughness may vary widely due to its lessened importance. In another example, the rehabilitation of pitted or oxidized surfaces via LIW cladding requires a thorough understanding of the relationship between changes in the

Table 1
Summary of prior investigations regarding the influence of surface irregularities on impact weld characteristics.

Author (year)	Impact weld process	Key details relevant to the present work
Godunov et al. (1970) [23]	Explosive welding (EXW) simulated; Cu/Fe	• Welds start only after the collision point travels a distance sufficient for destabilization. • Rarefaction waves forming behind shock fronts, and overtaking the advancing collision point, were seen as a major contributor to interfacial instabilities. • Experiments with a step machined into the target caused wavy interface formation immediately prior, confirming effect of rarefaction wave.
Szecket & Mayseless (1983) [24]	EXW; Cu/Cu, Steel/Steel	• Steps were machined into target plates in the experimental setup, with the geometry used to produce predictable instability leading to a weld. • In another experiment, strips embedded in the target plate with no changes in the profile caused predictable disturbances leading to a steady-state wavy interface.
Date et al. (1999) [25]	Kinetic impact welding; Al 1050 / Stainless Steel 304	• Welds were achieved between a pneumatically propelled flyer and fixed target parts within a vacuum chamber, at a zero relative collision angle. • Polished surfaces of average roughness values $R_a = 0.02$ μm and $R_a = 0.05$ μm both showed bonding, with the smoother surface profile resulting in a larger joint area. • However, the additional bonding area added negligible strength.
Bellmann et al. (2020) [12]	Kinetic impact welding; Al EN AW-1050 / Al ENAW-6060	• Aluminum targets were processed to surface roughness values of $R_a \sim 0.5$, 3.2, 7.8 μm, with flyers processed to $R_a \sim 0.5$ μm only, to study effect of surface roughness. • Increased surface roughness impeded the escape of the near-surface, high temperature cloud of particles from the collision point, trapped jet material in the weld for medium target roughness values, and no joint formation in the roughest samples.

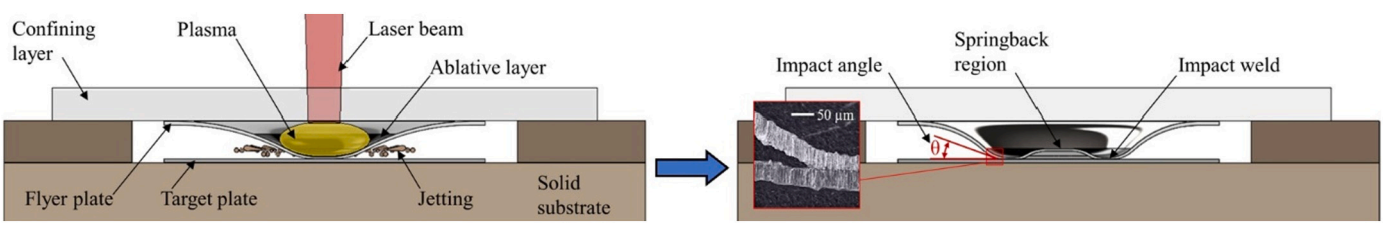

Fig. 1. (*Left*) Schematic of a laser impact welding process illustrating the expanding plasma that propels the flyer toward the stationary target. On impact, material jetting phenomena is observed. (*Right*) The resulting impact weld, featuring a springback region that develops [10]. (*Inset*) Optical micrograph featuring a cross section of an Al 1100 – SS 304 laser impact weld, adapted from an earlier publication by the authors [9].

roughness of the joined surfaces and the effectiveness of the impact welding process.

Moreover, as microelectromechanical industries would benefit particularly from improvements in microscale LIW, research toward using flyers as thin as 250 nm is increasingly important. Prior work by Frank et al. [28] demonstrated that such thin aluminum flyers can be successfully launched using pulsed lasers. Bellmann et al. [12] experimentally demonstrated that excessive surface roughness on such small-scale welds interrupts the contact between impacting surfaces and prevents the escape of jetted matter, impeding weld formation. However, the underlying phenomena occurring at the weld interface to explain such experimental observations could not be given. In earlier work by the authors [9,29], numerically predicted wave amplitudes in LIW interfaces of under 2 μm (i.e., comparable to the size of surface asperities found in commercial metal foils) were observed in models featuring homogeneous and inhomogeneous microstructures. The differences in weld behavior shown therein suggest that small, but destabilizing, features adjacent to the LIW collision point path affect the process, though surface asperities were not studied. Thus, it is yet to be determined (1) The extent to which a destabilization of the advancing collision point may be predicted when realistic surface profiles are incorporated in a numerical LIW process model; (2) The magnitude by which the overall surface roughness alters the transient thermal, strain, and shear stress characteristics of the developing weld. Accordingly, this work demonstrates a computational LIW framework that captures the effects of experimentally determined "realistic" (or rough) collision surfaces on the transient phenomena that emerge during joint formation. Section 2 describes the white light interferometry process used to acquire surface profile data that is subsequently imported into the physics-based LIW model. Section 3 presents the significant findings and discusses important phenomena predicted by the framework. Key concluding points of the work are given in Section 4.

2. Laser impact welding framework incorporating experimentally measured surface topography

LIW processes resolve on rapid timescales (~1 μs) and within very small characteristic dimensions, making in situ experimental observations of the evolution of stress, temperature, and plastic strain fields impractical. Thus, to investigate the evolving mechanisms of LIW interface formation, it is necessary to employ physics-based numerical formulations using constituent material models that are suitably calibrated [10]. The technique used to measure surface topography is described next, in Section 2.1. Section 2.2 provides a description of the Eulerian framework used and the layout of the simulation, including the parameters of an experimentally derived loading condition. Section 2.3 describes and lists parameters for the empirical material models used for the LIW model.

2.1. Surface topography measurement via white light interferometry

To elucidate the effects of the surface roughness on the LIW process, two separate finite element (FE) simulations are performed, one of which incorporates representative microscale geometry of the colliding surfaces for both an aluminum 1100-H19 (Al 1100) flyer foil and stainless steel 304-O (SS 304) target foil. The element length of the mesh used, 2 μm, limits the resolution of any surface profile data collected; therefore, a white light interferometry experiment suited to the spatial resolution of the computational model is used to collect the surface topography data. To convert the profile of each foil surface to a digital model, measurements are taken via a vertical scanning procedure using a Motic PSM-1000 optical microscope illuminating the sample with a white light source; photographs of the experimental setup are shown in Fig. 2a, with detail of the objective lens and a fringe pattern image provided in Fig. 2b and c, respectively. A Nikon objective lens of 10× lateral magnification and numerical aperture of 0.30 is mounted to a Newport NPO250SC nano-focusing stage containing a piezoelectric transducer actuated by a Newport NPC3SG controller in closed-loop mode. A Moticam digital camera, operating in 1024 × 768 resolution mode with 0.61 μm square pixels, captures fringe patterns in vertical scan increments of 0.1 μm over a total distance of 10 μm. A single vertical distance along the Y-axis corresponding to maximum brightness in the fringe pattern is found for each pixel using digital image analysis. Combined with the use of calibration slides to scale the images, 3D profiles of the foil surfaces are constructed.

As the interferometry procedure requires significant reflections from a sampled surface for best accuracy, the more reflective sides of the sampled Al 1100 and SS 304 foils are used for the measurements. Also, since the computational model used in this study is based on a 2D layout of the LIW process, for consistency profiles are sampled from lines parallel to the highly visible groove patterns in both materials. For the Al 1100 flyer surface, the average roughness (R_a) measurement is 0.5 μm, maximum peak-to-valley (R_Y) is 4.5 μm, and standard deviation (R_{dev}) is 0.63 μm. For the SS 304 target surface, these quantities are 0.3 μm, 3.2 μm, and 0.37 μm, respectively. Skewness (R_{sk}) for the flyer foil is 0.03, indicative of an evenly distributed profile above and below the mean

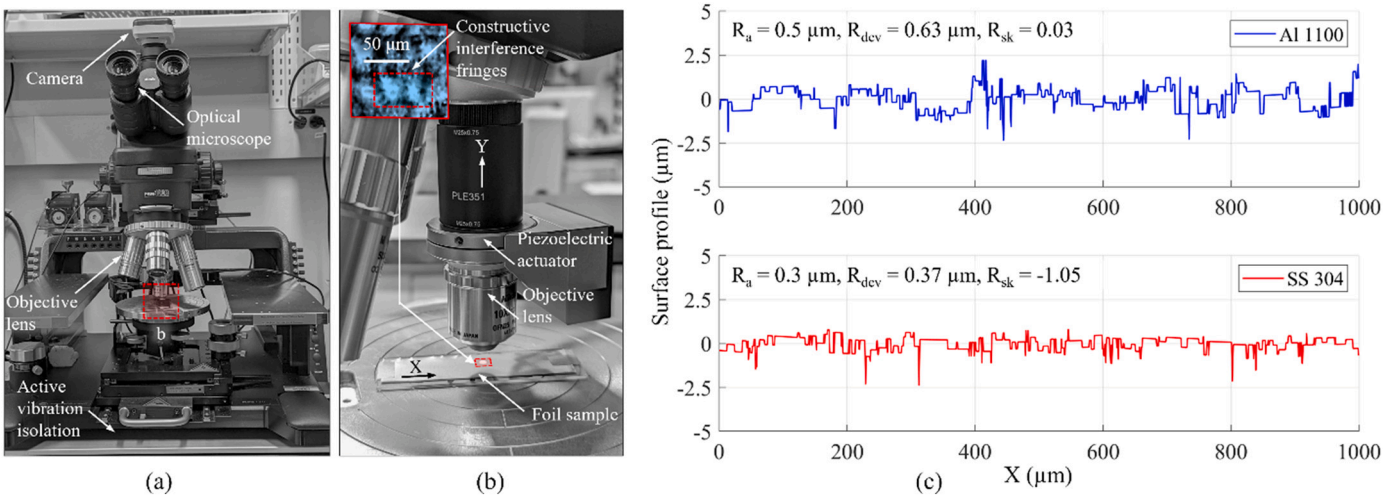

Fig. 2. (a) Photograph of the optical microscope for white light interferometry. (b) Detailed view of a stainless steel 304 foil sample and objective lens with piezoelectric actuator. (*Inset*) A sample of the acquired fringe pattern revealing high brightness zones resulting from constructive light interference. (c) Measured surface profile data for (Top) Al 1100 flyer, (Bottom) SS 304 target.

value. In contrast to the flyer's profile, the target's profile consists of a surface of broad plateaus and intermittent, deep, narrow valleys. In conjunction with the target foil's lower R_a, its skewness (R_{sk}) of −1.05 reveals a functionally smoother surface relative to that of the flyer. The acquired surface profiles are subsequently imposed on the contacting surfaces within the LIW model.

2.2. Physics-based laser impact welding model

LIW subjects solid materials to extreme shear deformations and local high temperatures that cause a fluidlike behavior at the collision interface, for which the Eulerian computational framework is well-suited [30]. By not explicitly meshing part surfaces, the Eulerian framework avoids mesh errors that are encountered when using Lagrangian or Arbitrary Lagrangian-Eulerian frameworks to track solution variables at a deforming weld interface [30,31]. The mesh-free smoothed particle hydrodynamics (SPH) method has also been used for computational modeling of impact welds for these reasons [22,32]. However, the static Eulerian mesh confers an additional benefit: it allows the modeling of partial material volume fractions within individual elements. This is needed to represent the experimentally obtained surface roughness, which have smaller characteristic length scales than the cubic elements of the Eulerian grid.

Eqs. (1) to (5) describe the multi-material Eulerian formulation used in the finite element LIW model [33]. The first three, Eqs. (1) to (3), describe conservation of mass, momentum, and energy within the domain, respectively. Terms $\dot{\boldsymbol{X}}$, $\boldsymbol{\sigma}$, $\dot{\varepsilon}_p$, t, and e, represent the velocity vector, stress tensor, plastic strain rate tensor, time, and internal energy per unit volume, respectively.

$$\frac{\partial \rho}{\partial t} + \nabla \cdot \left(\rho \dot{\boldsymbol{X}} \right) = 0 \tag{1}$$

$$\frac{\partial \rho \dot{\boldsymbol{X}}}{\partial t} + \nabla \cdot \left(\rho \dot{\boldsymbol{X}} \otimes \dot{\boldsymbol{X}} \right) = \nabla \cdot \boldsymbol{\sigma} \tag{2}$$

$$\frac{\partial e}{\partial t} + \nabla \cdot \left(e \dot{\boldsymbol{X}} \right) = \boldsymbol{\sigma} : \dot{\boldsymbol{\varepsilon}}_p \tag{3}$$

After performing an operator split, Eqs. (1) to (3) may be generalized in the form of Eqs. (4) and (5), where Ψ is a flux function, S is a source function, $\boldsymbol{X}$ is the position vector, and ϕ is a solution variable.

$$\frac{\partial \phi}{\partial t} = S \tag{4}$$

$$\frac{\partial \phi}{\partial t} + \nabla \cdot \Psi \left(\phi, \dot{\boldsymbol{X}}, \boldsymbol{X}, t \right) = \boldsymbol{0} \tag{5}$$

During each time increment, Eq. (4) is solved using a material derivative on a temporary Lagrangian mesh, instead of the spatial derivative shown; a sufficiently small time-increment is chosen to prevent displacement of solution variables across more than one element length, allowing the solution variable to be remapped onto the stationary Eulerian grid. The time increment ranges in duration from 1.621×10^{-10} s to 2.267×10^{-12} s during the run time of the dynamic explicit numerical models used in this work. Eq. (5) then accounts for advection effects, allowing equivalent plastic strain, internal energy, and material volumes to be tracked throughout the modeled LIW process.

The FE LIW model described in this subsection is based on an earlier experiment documented by the authors in which an impact weld between Al 1100 and SS 304 foils was formed and subsequently tested to a lap shear strength of 13.76 N [9]. These foils were sourced from the same supplier (McMaster-Carr) and met the same alloy composition and heat treatment specifications as the foils characterized by the interferometry experiments described in Section 2.1. The numerical model emulating the initial layout of this experiment is shown in Fig. 3. Linear hexahedral elements with cubic edge lengths $L_e = 2$ μm are used in the Eulerian mesh, and feature thermal, translational, and rotational degrees of freedom with reduced integration, considering the computational intensiveness. The SS 304 target foil is modeled within the Eulerian domain entirely, with a 50 μm total nominal thickness. The Al 1100 flyer foil, however, is decomposed into an Eulerian domain of 46 μm nominal thickness relative to the surface to be welded, and a Lagrangian domain in the top 4 μm from the upper loading surface. Splitting the representation of the part allows for a realistic plasma pressure load to be applied directly to the upper Lagrangian surface of the flyer and does not significantly affect the near-interface phenomena predicted during the simulation. This Lagrangian surface is thus omitted for clarity from the predicted results presented and discussed later in Section 3. An aluminum A357 substrate upon which the target foil initially rests is modeled using shell elements with initial orientation aligned with the XZ-plane. A section thickness much greater than that of the foils (6.35 mm) is assigned, with a simple pin condition applied to the far end (X = 1.1 mm). The radial length of the modeled foils is 1 mm, which accommodates the extent of welds observed in LIW experiments.

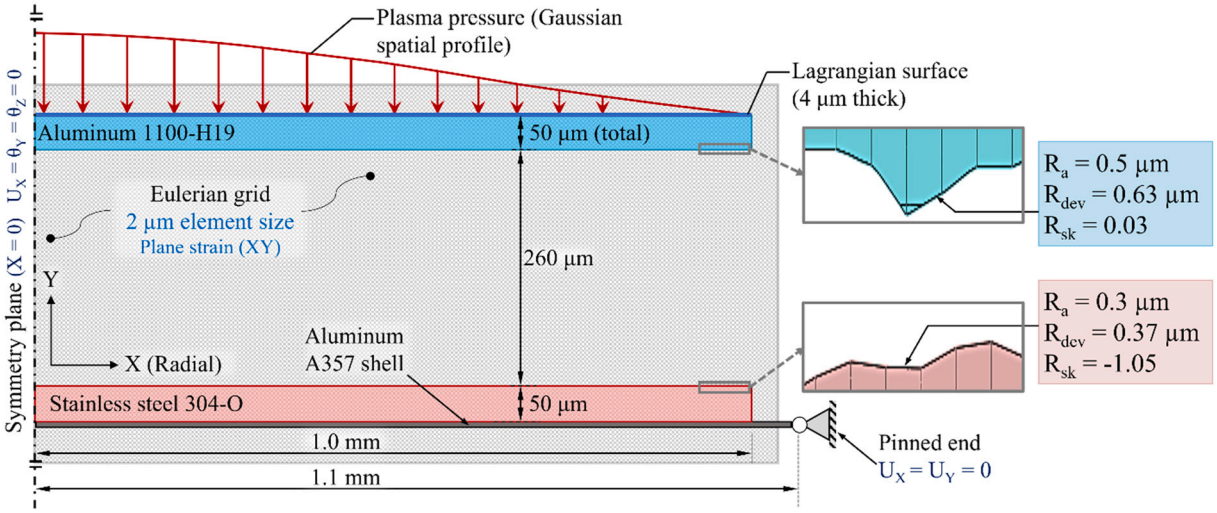

Fig. 3. (*Left*) A schematic of the LIW model used to emulate experiments documented in [9], showing the plasma pressure profile used. (*Right*) The acquired surface profiles shown for the flyer and target (with roughness values indicated), as modeled within the Eulerian mesh, are implemented in the rough surface model (scale of surface profiles in the Y-direction of the insets has been increased by a factor of 4 for clarity).

A standoff distance of 260 μm separates the flyer and target surfaces, which is consistent with successful welds observed in LIW experiments. To conserve computational resources, no material is assigned in the Eulerian mesh outside of the solid parts, and a symmetry condition is applied at X = 0 mm ($U_x = \theta_y = \theta_z = 0$) to all modeled materials and parts. Additionally, the entire model is constrained by a plane strain condition ($U_z = \theta_x = \theta_y = 0$) throughout, with an out-of-plane model depth of 4 μm in the inactive Z-direction. The resulting FE model is representative of a radially symmetric, 2D LIW process.

For the case in which topography of the impacting surfaces is neglected, the geometry of the smooth surface model is described exclusively by rectangular extrusions for the flyer and target. In contrast, for the new rough surface model, profiles of the contacting surfaces of the Al 1100 and SS 304 foils are imported from the dataset collected via interferometry. The average surface height (in the Y-direction) is aligned with the nominal thickness of each foil. A Python scripting routine is used to import datapoints that digitally stitch together the experimentally acquired surface profile along the length of each modeled foil. Thus, the experimentally measured rough surfaces are closely replicated within the Eulerian model. Surfaces that remain modeled as continuous and smooth planes include the surfaces on the foils opposite to those comprising the weld interface, the surface plane of symmetry at X = 0 mm, and the vertical foil surfaces at X = 1 mm.

A laser-induced plasma pressure pulse that varies both with radial distance from the spot center (X = 0 mm) and with time is imposed as the loading condition on the top surface of the Al 1100 flyer foil. For the temporal profile, a transient piecewise continuous function of the pressure at the spot center is applied based on differential equation solutions to a confined ablation model by Fabbro et al. [34]. These solutions are given by Eq. (6) and are plotted in Fig. 4; the heating phase $t < t_p$ terminates at a peak pressure of 2.4 GPa, and an adiabatic cooling phase follows, applying a monotonically decreasing load until it reaches 10 % of the peak value at $t = 340$ ns, at which point it is set to zero due to negligible continued effect on the LIW process (collision occurs at approximately 300 ns). In Eq. (6), α represents the portion of laser energy converted to thermal energy, λ is the adiabatic index of the plasma, Z is the shock impedance of the system, L_0 is the initial plasma thickness, I_0 is the laser pulse energy flux, and $L(t)$ is the plasma thickness with respect to time.

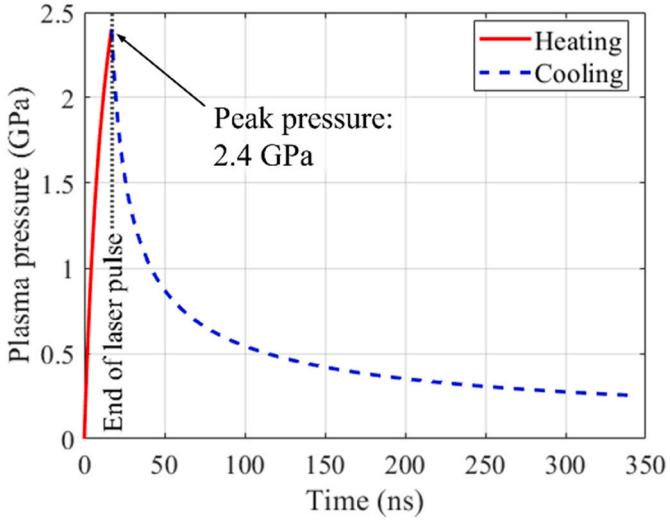

Fig. 4. Piecewise continuous temporal profile of the applied plasma pressure load, as imposed at the spot center.

$$P(t) = \begin{cases} \frac{1}{10}\left\{\left[\frac{\alpha Z I_0}{2\alpha+3}\right]\left[1-\left(\frac{L_0}{L(t)}\right)^2\right]\right\}^{\frac{1}{2}}, \text{for } t < t_p \\ P(t_p)\left[\frac{L(t_p)}{L(t)}\right]^{\lambda}, \text{for } t \geq t_p \end{cases} \quad (6)$$

The shock impedance coefficient, Z, requires the combination of the impedance values for the Al 1100 flyer foil (Z_{Al}) and the borosilicate glass confining layer (Z_g) (ref. Fig. 1), and is calculated by Eq. (7). Values used for the hydrodynamic model are listed in Table 2.

$$Z = \frac{Z_{Al} Z_g}{2(Z_{Al} + Z_g)} \quad (7)$$

The axisymmetric pressure distribution is based on characterization of the spatial energy distribution of a Q-switched laser pulse by Hatamleh et al., in which a 3D point cloud, revealing the intensity of the laser radiation with respect to the spot center, was collected using a beam profiling camera [35]. After mapping the 3D point cloud to radial distance X from the spot center (X = 0 mm), a Gaussian curve fit to the data is used to represent the pressure distribution in the Eulerian plane strain model. These laser pulse characterization experiments also provide the FWHM pulse width and averaged laser pulse flux found in Table 2. Scaling the distribution by the peak pressure at the spot center results in a more realistic velocity profile and flyer deformation during the early stages of the LIW simulation [29]. The spatial data curve fit is described by Eq. (8), with the standard deviation, $\Omega_X = 0.399$ mm, derived from the 3D point cloud data distribution from the spot center.

$$P(X) = \frac{1}{\Omega_X \sqrt{2\pi}} e^{-\frac{1}{2}\left(\frac{X}{\Omega_X}\right)^2} \quad X \geq 0 \quad (8)$$

2.3. Material modeling

To accommodate the extreme strain rates and elevated temperatures that emerge during impact weld processes [16], the numerical model incorporates a Johnson-Cook plasticity model inclusive of strain, strain rate and temperature dependence. Flow stress, σ_f, is expressed in terms of the current plastic strain ε_p, plastic strain rate $\dot{\varepsilon}_p$, and homologous temperature T^* as defined by Eqs. (9) and (10).

$$\sigma_f = \left[A + B(\varepsilon_p)^n\right]\left[1 + C\, ln\left(\frac{\dot{\varepsilon}_p}{\dot{\varepsilon}_0}\right)\right]\left[1 - (T^*)^m\right], \quad \text{for } t \geq 0 \quad (9)$$

$$T^* = \begin{cases} 0 & \text{for } T < T_0 \\ \left(\frac{T - T_0}{T_m - T_0}\right) & \text{for } T_0 \leq T \leq T_m \\ 1 & \text{for } T > T_m \end{cases} \quad (10)$$

The high pressure exerted by the pulsed laser-induced plasma requires the use of a thermodynamic equation of state (EoS). Since the metallic materials used have large bulk moduli and adiabatic index under ambient conditions, and the shock pressures of interest are well below ~100 GPa, the entropy increase is small [37]. Thus, a Mie-

Table 2
1D Hydrodynamic model parameters [34–36].

Hydrodynamic model parameter	Value
FWHM pulse width, t_p	17 ns
Averaged laser pulse flux, I_0	1.8 GW cm^{-2}
Energy ratio, α	0.25
Adiabatic index, λ	1.4
Glass shock impedance, Z_g	1.14×10^6 g cm^{-2} s^{-1}
Al shock impedance, Z_{Al}	2.75×10^6 g cm^{-2} s^{-1}
Initial plasma thickness, L_0	10 μm

Grüneisen EoS, given by Eq. (11), is used to describe the dynamic relationship of volumetric stress (pressure p) and strain (volume) during the LIW process. η is the ratio of U_p to U_s, E_m is the specific internal energy per unit mass, s is a dimensionless constant, ρ_0 is reference density, and Γ is a dimensionless Grüneisen parameter capturing thermodynamic response.

$$p = \frac{\eta\rho_0 {c_0}^2}{(1-s\eta)^2}\left(1-\frac{\eta\Gamma}{2}\right)+\Gamma\rho_0 E_m \tag{11}$$

A Hugoniot linear function, Eq. (12), relates the shock wave velocity U_s to the particle velocity U_p, where c_0 is the bulk speed of sound in the material.

$$U_s = c_0 + sU_p \tag{12}$$

Eq. (13) captures the elastic deviatoric stress-strain response of each foil, where $\boldsymbol{\sigma_d}$ is the deviatoric stress, G is the elastic shear modulus, and $\boldsymbol{\varepsilon_{el}}$ s the deviatoric elastic strain. All the LIW material constitutive model parameters are given in Table 3.

$$\boldsymbol{\sigma_d} = 2\mathrm{G}\boldsymbol{\varepsilon_{el}} \tag{13}$$

To reduce unrealistic rebound of the foils post-collision, a deformable substrate beneath the target foil is described using a greatly simplified isotropic linear elastic and linear plastic material model of aluminum alloy A357, with details given in Table 4. The model notably omits strain rate sensitivity, an EoS, and coupling of temperature and mechanical effects to limit computational expense.

The thermomechanical model considers a 90 % fraction of the plastic work, $\boldsymbol{\sigma} : \dot{\boldsymbol{\varepsilon}}_p$, to be converted to heat, thereby permitting endothermic phase change effects to account for the balance of change in internal energy, e (ref. Eq. (3)). Results predicted from the LIW simulations comparing the effects of the inclusion of surface topography on the transient interfacial phenomena, are discussed next, following Fig. 5 that summarizes the modeling framework.

3. Results and discussion

The temperature distributions at initial collision (t = 305 ns) between the flyer and target foils are depicted in Fig. 6. Fig. 6a offers a quantitative comparison of peak temperatures along the collision interface in the rough and smooth surface models. A peak of 1680 K at the spot center (X = 0 mm), along with a generally elevated thermal profile along the contacting surfaces, distinguishes the interfacial thermal behavior of the rough surface model from the smooth. Without the presence of surface asperities to localize shock compression in the central region where the collision angle is near zero, the smooth surface model peaks at 918 K at X = 0.06 mm, elevated from 856 K at the spot center. Major differences are predicted in the behavior of the colliding foils based on the modeling of surface roughness; peak T_{rough} is just above the melting point of the SS 304 target, while peak T_{smooth} only reaches just above the significantly lower melting point of the Al 1100 at a different location; this gradual increase away from the spot center to X = 0.06 mm is a likely result of the effects of plastic dissipation increasing as the angle begins to increase at the collision point. The high temperatures predicted between the rough surfaces suggest the formation of discontinuous fusion welds at the spot center due to adiabatic shock compression alone. However, surface impurities, trapped air, and elastic rebound effects inhibit the formation of a successful weld near the spot center (X < 0.29 mm); additionally, the latter two effects have not been included in the demonstrated modeling framework. Fig. 6b and c qualitatively depict the temperature distribution in the region near the modeled collision interfaces, and reveal the forming collision point that is similarly located in both models at X = 0.077 mm. Fig. 7 qualitatively depicts the temperature distribution in the region near the modeled collision interfaces as the collision point travels away from the spot center, and collision angle increases. Prior to weld formation (t = 320 ns), adiabatic shock compression effects dominate, with peak temperatures near the collision point reaching 2235 K in the rough surface model, and 2316 K in the smooth surface model. Temperatures exceeding 1000 K trail the collision point by 50 μm in the rough surface model, and by 14 μm between the smooth surfaces (ref. Fig. 7a, c), indicative of interrupted contact between rough surfaces reducing the dissipation of the local adiabatic heating. Just above and below the collision zone, the flyer and target show rapidly advancing shock fronts, marked by elevated temperature, that are less pronounced between rough surfaces than smooth ones, and are more noticeable in both models' Al 1100 flyer rather than the SS 304 target. The effects of surface topography concentrate applied dynamic stresses among a distribution of peaks, contributing to increased plastic dissipation in the flyer that effectively dampens the internal elastic stress shockwave, particularly within the flyer. Reflected elastic shock waves are also seen propagating from the substrate at this time in both models, though the thermal effects of these rapidly begin to dissipate. Despite temperatures well above both materials' melting points at the interface from 320 ns ≤ t < 345 ns, no weld formation is predicted until the end of this interval. The Eulerian framework used in the numerical model has a notable disadvantage relative to a Lagrangian method in that material surfaces of parts must be interpolated within the static mesh and impacting surfaces cannot separate. Therefore, mutual ablation of the colliding surfaces, forming a jet, is the necessary criterion to ascertain the times and locations at which an impact weld is formed. Thus, the jetting predicted in Fig. 7b, d (t = 345 ns) indicates the initiation of weld formation in the rough and smooth surface models, respectively; the rarefaction wave trailing the initial shock front has overtaken the advancing collision point, causing instabilities that remove surface material, consistent with interpretations of observations by Godunov et al. [23]. Concurrently, temperatures decline near the collision point, with peak values of 1612 K and 1621 K in the rough and smooth models, respectively (ref. Fig. 7b, d). Contact between the surfaces in both rough and smooth cases becomes more uniform as the collision angle increases moving away from the spot center. As a result, thermal conduction at the interface is now similar between the models, with temperature fields becoming less distinguishable past X = 0.184 mm, both at the collision interface and at the internal shock fronts. Plastic deformation at the LIW interface modeled using rough surfaces is compared with the model using the smooth surfaces in Fig. 8, that illustrates equivalent plastic strain values at the key time frames of 345, 450, and 800 ns. In the rough surface

Table 4
Material model for aluminum alloy A357 substrate [42].

Density, ρ_0	Young's modulus	Poisson's ratio	Compressive yield stress	Ultimate compressive strength
2670 kg m^{-3}	72.4 GPa	0.33	241 MPa	310 MPa

Table 3
Laser impact welding material model parameters for Al 1100 and SS 304 foils [38–41].

	Johnson-Cook plasticity model								Hugoniot equation of state				
	A (MPa)	B (MPa)	C	$\dot{\varepsilon}_0$ (s^{-1})	n	m	T_0 (K)	T_m (K)	ρ_0 (kg m^{-3})	c_0 (m s^{-1})	s	Γ	G (GPa)
Al	148.4	345.5	0.001	1	0.183	0.895	293	916	2712	5451.8	1.2592	2.14	27.4
SS	110	1500	0.014	1	0.014	1	293	1673	7905	4722	1.441	1.93	78

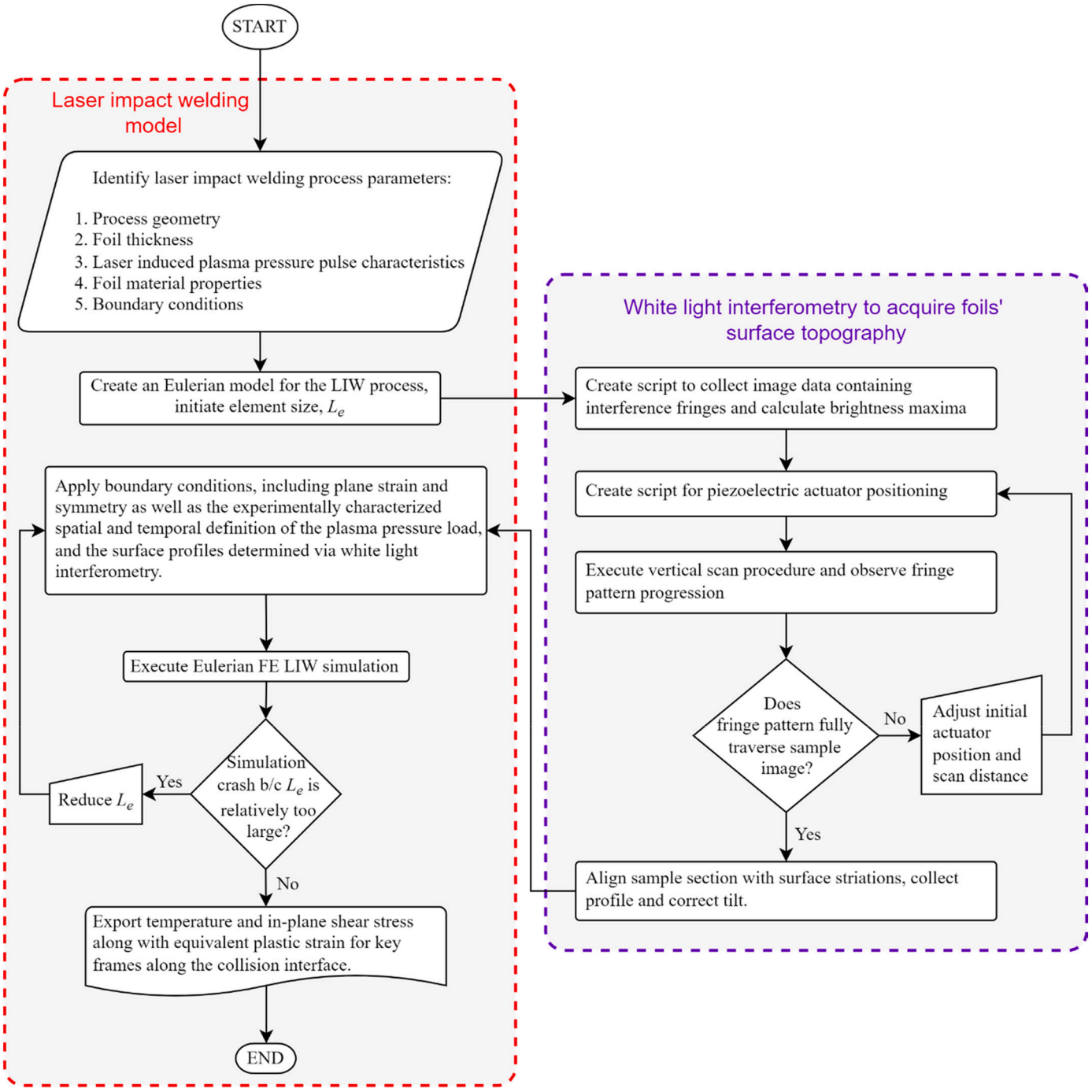

Fig. 5. Flowchart offering an overview of the modeling framework for LIW of metallic foils, incorporating the surface topography measured via white light interferometry.

model, peak equivalent plastic strain (ε_{eq}) reaches 2.91 just prior to the emergence of the jet ($t = 345$ ns); similarly, the smooth surface model reaches a peak ε_{eq} of 2.9; combined with the similar profiles plotted in Fig. 8a, minimal overall differences in interfacial plastic deformation due to surface topography are indicated. The first frame, $t = 345$ ns, shows the initiation of jetting at X = 0.3 mm in the rough surface model, and X = 0.298 mm in the smooth surface model. Fig. 8b indicates a zone of intermittent contact toward the weld center in the rough surface model, X < 0.12 mm, containing voids after the initial collision (Zone 1). This suggests insufficient shear forces are present during initial impact, with elastic rebound occurring between surface asperities, resulting in interrupted contact between the flyer and target that would not yield a strong weld, even under vacuum conditions between surfaces free of contaminants [25]. In the interval 0.12 < X < 0.29 mm in the rough surface model (Zone 2), plastic deformation begins to localize at the interface, and surface features begin to flatten via shear effects to a depth greater than the maximum roughness values of the flyer and target surfaces. As a result, interfacial voids no longer appear. Note these transient phenomena occur prior to the formation of the jet and would be very difficult (if not impossible) to observe experimentally.

At $t = 450$ ns, the jetting process is underway in both LIW models, indicating continued weld formation (Fig. 8e, f); differences in the interfacial plastic strain between the rough and smooth surface models are more apparent here (Fig. 8d) than in the initial phase. The rough

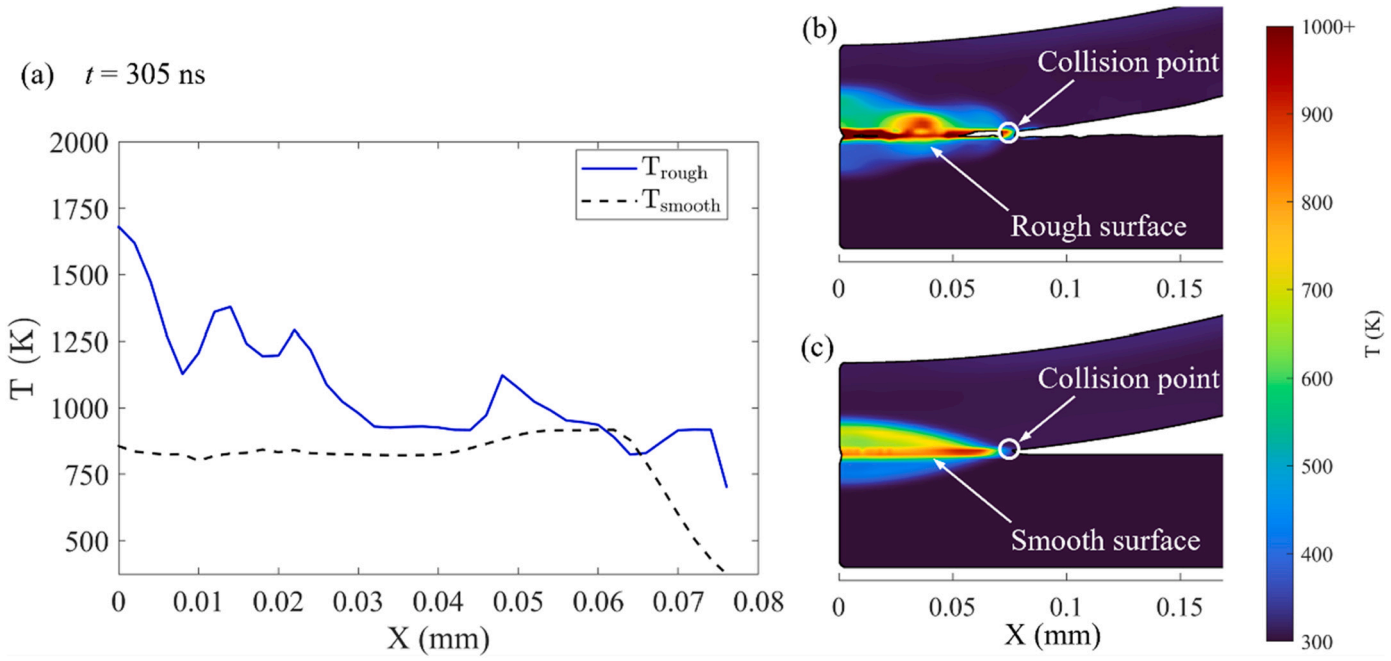

Fig. 6. For time $t = 305$ ns: (a) Peak temperatures along the collision interface. (b) Temperature distribution near the contact region for rough surface model and (c) smooth surface model. (For interpretation of the reference to color in this figure, the reader is referred to the online version of this article.)

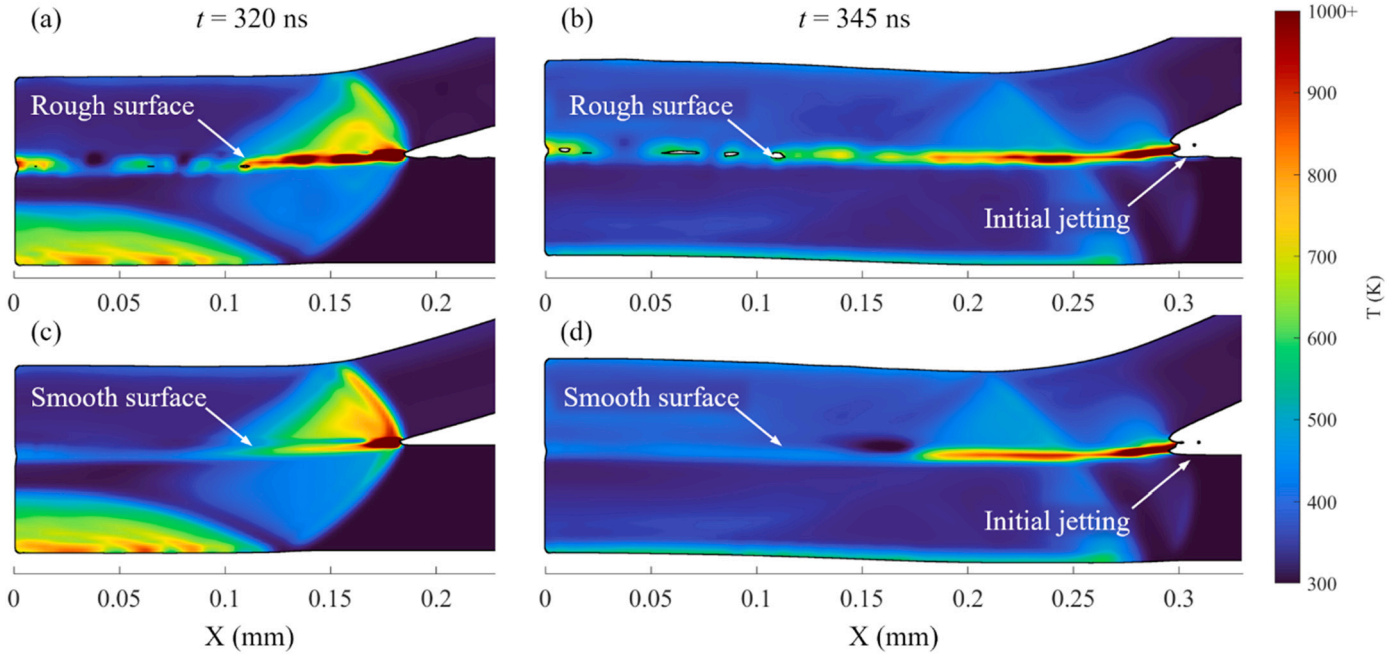

Fig. 7. Temperature distribution within the colliding foils for the rough surface model at times (a) $t = 320$ ns and (b) $t = 345$ ns. Corresponding temperature distribution within the colliding foils for the smooth surface model at times (c) $t = 320$ ns and (d) $t = 345$ ns. (For interpretation of the reference to color in this figure, the reader is referred to the online version of this article.)

surface model shows decreased interfacial plastic strain compared to the smooth surface model in the region $0.388 < X < 0.488$ mm, indicative of a reduced strain threshold needed for material to be jetted. Bellmann et al. [12] observed no jet entrapment inhibiting the weld formation on aluminum impact weld samples at lower roughness values ($R_a = 0.5$ μm); likewise here, the weld process is unimpeded by the incorporation of flyer and target surface profiles.

At $t = 800$ ns, no further jetting emerges from the collision point and the weld formation process terminates; here, the greatest difference in ε_{eq} is established at the outermost region, from $0.598 < X < 0.694$ mm. In the smooth and rough surface models, respectively, ε_{eq} peaks at 16.1 and 12.1, respectively, at the end of the weld region. The interruption of contact at the welding interface, with unstable motion of the collision point in the vertical (Y) direction offers a plausible explanation for this difference in ε_{eq} for the region $X > 0.6$ mm. Overall, the incorporation of surface profiles affects the development of plastic strains toward the end of the weld, but does not substantially affect weld initiation in the same manner as the placement of edge disturbances orthogonal to the

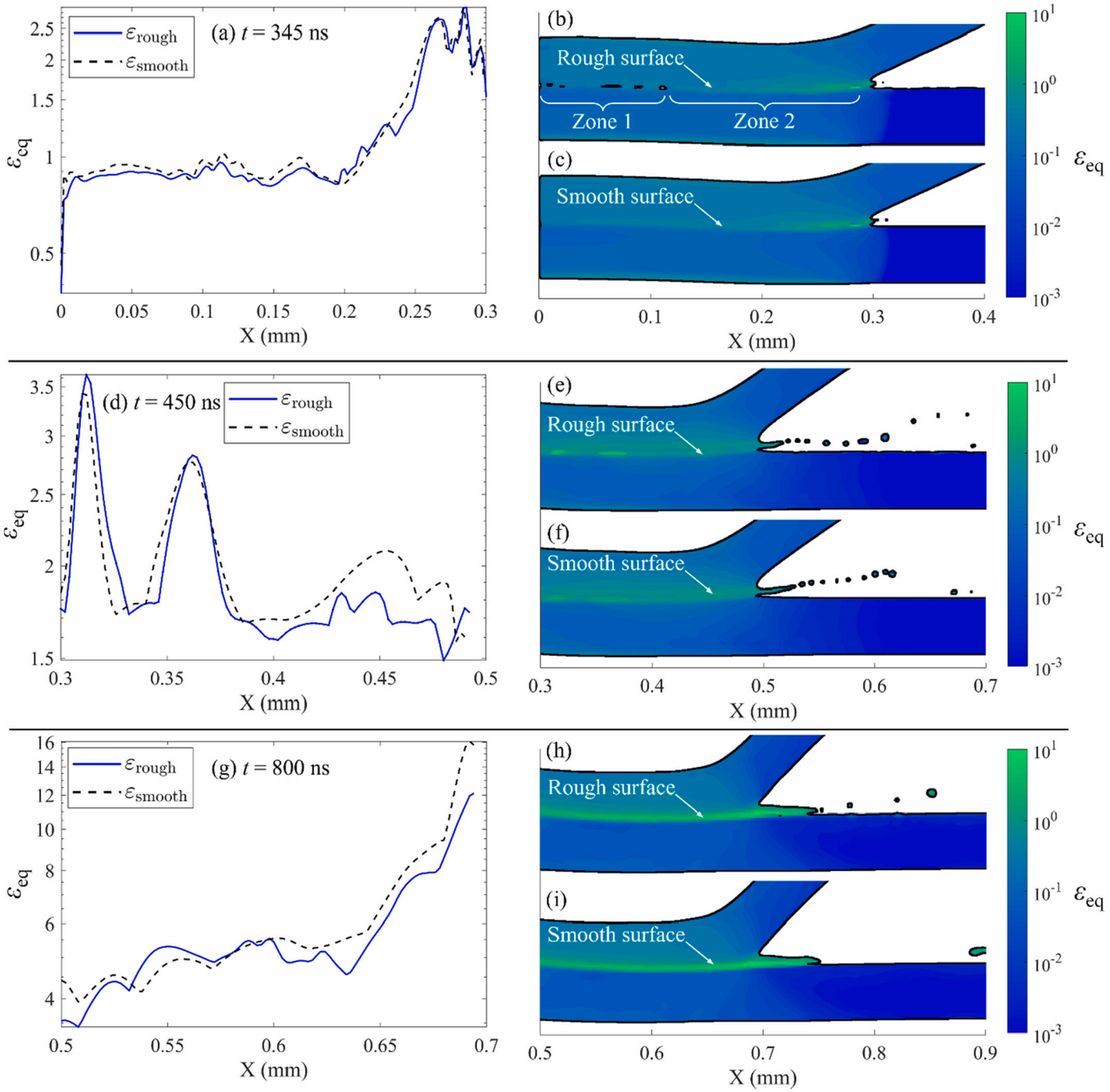

Fig. 8. (Left) Comparison of peak equivalent plastic strains (ε_{eq}) along the collision interface for rough and smooth surface models at times (a) $t = 345$ ns, (d) $t = 450$ ns, and (g) $t = 800$ ns. (Right) Corresponding ε_{eq} distribution within the colliding foils for (b, e, and h) the rough surface model and (c, f, and i) the smooth surface model during the highly dynamic weld formation. (For interpretation of the reference to color in this figure, the reader is referred to the online version of this article.)

collision point's travel [24].

A comparison of the in-plane shear stresses predicted during the initial contact ($t = 305$ ns) of the foils, presented in Fig. 9, reveals significant differences in the shear stress fields between the rough and smooth surface models. The emerging shear stress field depicted in Fig. 9a show concentrations of opposing stress magnitudes that are not substantially localized at the collision point due to the shallow angle between the colliding foil surfaces. The maximum and minimum shear stresses of 385 MPa and − 286 MPa, respectively, are both found in the SS 304 target, with a distribution that is not conducive to the mutual surface ablation needed for weld formation. As the SS 304 contact surface is substantially smoother and with a greater yield strength than the flyer's, much of the impact energy is dissipated via heating from adiabatic shock and subsequent rebound at the central region. However, for the remainder of the LIW process, the shear stress fields do not differ significantly between the models.

4. Conclusions

To improve the prospects of industrial adoption for the LIW process, considerations must be made for micro-scale features, including surface topography, that may affect the process repeatability in joints formed between thin metallic foils. The Eulerian computational framework demonstrated in this work investigates the influence of experimentally

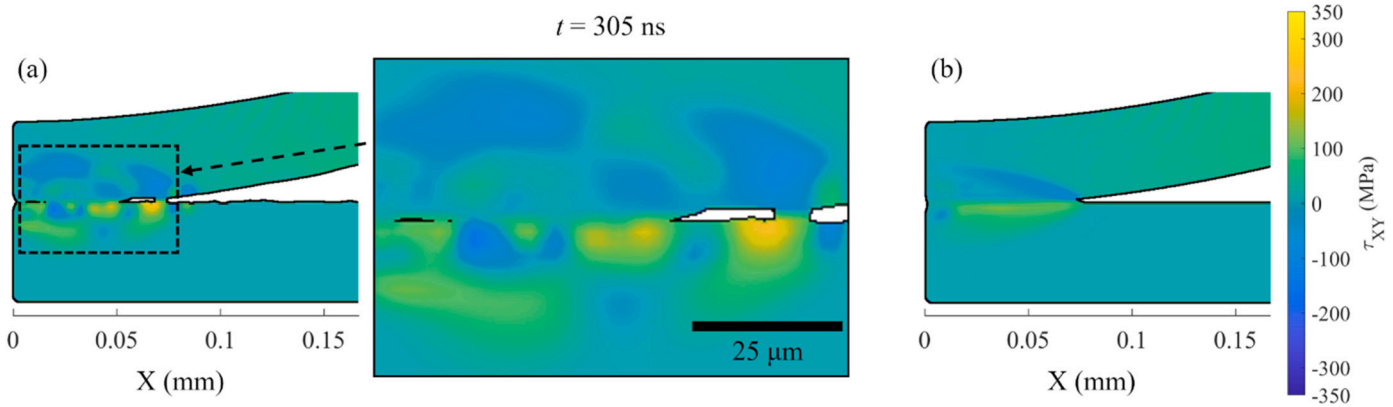

Fig. 9. Shear stress distribution within the foils near the collision interface at $t = 305$ ns for (a) the rough surface model, and (b) the smooth surface model. (For interpretation of the reference to color in this figure, the reader is referred to the online version of this article.)

measured surface roughness on the LIW process between dissimilar materials, including comparisons of temperature, plastic strain, and shear stress before, during, and after weld formation. This study illuminates the predicted effects that surface topography has on the transient phenomena emerging during LIW for the case in which maximum peak- to-valley distances are on the same order of magnitude of the foil thicknesses. Key findings are summarized as follows:

- Significantly higher temperatures just beyond the melting point of SS 304 occur between rough surfaces due to the intermittent contact of asperities during initial collision. In the model with no surface topography included, temperatures only slightly exceed the Al 1100 melting point, and greatly reduced thermal profiles trail the collision point. These results indicate that limited contact between rough surfaces prior to weld formation results in more extensive heat affected zones than if the surfaces are assumed to be perfectly smooth.
- Plastic deformation is substantially reduced at the rough LIW interface in contrast to the smooth interface, with the greatest differences toward the outer region of the weld, suggesting reduced available energy for mutual surface ablation when accounting for surface features.
- Shear stress effects are largely unchanged due to the presence of measured surface profiles, with the only notable differences in the stress fields emerging during initial contact. The concentration of opposing shear stresses at the collision point, combined with elevated temperatures, cause the inclusion of surface asperities in the numerical model to have minimal stress effects, with the mechanical distinctions between the rough and smooth surface models being largely revealed through comparison of strain profiles.
- Contact between the foils is inconsistent between rough surfaces, which allows additional interfacial characterization in the thermomechanical modeling of the LIW process. A minimally deformed central rebound zone, featuring voids between the surfaces, can be distinguished from a moderately deformed zone where superficial shear deformation occurs prior to the start of jetting and the formation of the weld. The softer Al 1100 flyer material yields to initiate a continuous contact zone, indicating a plausible prerequisite condition for joint formation in LIW—an uninterrupted, mutually shearing collision point prior to surface ablation.

Declaration of competing interest

The authors declare that they have no known competing financial interests or personal relationships that could have appeared to influence the work reported in this paper.

Acknowledgment

A. Malik acknowledges partial support from the U.S. National Science Foundation, grant no. CMMI-1762722. Any opinions, findings, or conclusions expressed in this paper are those of the authors and do not necessarily reflect the views of the U.S. National Science Foundation. R. A. Bernal acknowledges support from The University of Texas at Dallas.

References

[1] Cai W, Daehn G, Vivek A, Li J, Khan H, Mishra RS, Komarasamy M. A state-of-the-art review on solid-state metal joining. J Manuf Sci Eng 2019;141:031012.
[2] Groche P, Becker M, Pabst C. Process window acquisition for impact welding processes. Mater Des 2017;118:286–93.
[3] Liu W, Wang H-P, Lu F, Cui H, Tang X. Investigation on effects of process parameters on porosity in dissimilar Al alloy lap fillet welds. Int J Adv Manuf Technol 2015;81:843–9.
[4] Wang C, Cui L, Mi G, Jiang P, Shao X, Rong Y. The influence of heat input on microstructure and mechanical properties for dissimilar welding of galvanized steel to 6061 aluminum alloy in a zero-gap lap joint configuration. J Alloys Compd 2017;726:556–66.
[5] Xiong L, Cheng J, Chuang AC, Hu X, Sun X, Singh D. Synchrotron experiment and simulation studies of magnesium-steel interface manufactured by impact welding. Mater Sci Eng A 2021;813:141023.
[6] Wang H, Wang Y. High-velocity impact welding process: a review. Metals 2019;9:144.
[7] Wang X, Zhang H, Shen Z, Li J, Qian Q, Liu H. Experimental and numerical investigation of laser shock synchronous welding and forming of copper/aluminum. Opt Lasers Eng 2016;86:291–302.
[8] Wang X, Huang T, Luo Y, Liu H. Laser indirect shock welding of fine wire to metal sheet. Materials 2017;10:1070.
[9] Sadeh S, Gleason GH, Hatamleh MI, Sunny SF, Yu H, Malik AS, Qian D. Simulation and experimental comparison of laser impact welding with a plasma pressure model. Metals 2019;9:1196.
[10] Wang X, Tang H, Shao M, Jin H, Liu H. Laser impact welding: investigation on microstructure and mechanical properties of molybdenum- copper welding joint. Int J Refract Met Hard Mater 2019;80:1–10.
[11] Crossland B, Bahrani A. Fundamentals of explosive welding. ContempPhys 1968;9:71–87.
[12] Bellmann J, Lueg-Althoff J, Niessen B, Böhme M, Schumacher E, Beyer E, Leyens C, Tekkaya AE, Groche P, Wagner MF-X, et al. Particle ejection by jetting and related effects in impact welding processes. Metals 2020;10:1108.
[13] Walsh J, Shreffler R, Willig F. Limiting conditions for jet formation in high velocity collisions. J Appl Phys 1953;24:349–59.
[14] Robinson J. Fluid mechanics of copper: viscous energy dissipation in impact welding. J Appl Phys 1977;48:2202–7.
[15] Cowan G, Bergmann O, Holtzman A. Mechanism of bond zone wave formation in explosion-clad metals. Metall Mater Trans B 1971;2:3145–55.
[16] Robinson J. The mechanics of wave formation in impact welding. Philos Mag 1975;31:587–97.
[17] Hay D. Explosive welding: applications and techniques. In: High-pressure science and technology. Springer; 1979. p. 1813–36.
[18] Vivek A, Liu BC, Hansen SR, Daehn GS. Accessing collision welding process window for titanium/copper welds with vaporizing foil actuators and grooved targets. J Mater Process Technol 2014;214:1583–9.
[19] Bataev I, Tanaka S, Zhou Q, Lazurenko D, Junior AJ, Bataev A, et al. Towards better understanding of explosive welding by combination of numerical simulation and experimental study. Mater Des 2019;169:107649.

[20] Nassiri A, Vivek A, Abke T, Liu B, Lee T, Daehn G. Depiction of interfacial morphology in impact welded Ti/Cu bimetallic systems using smoothed particle hydrodynamics. Appl Phys Lett 2017;110:231601.
[21] Lee T, Zhang S, Vivek A, Kinsey B, Daehn G. Flyer thickness effect in the impact welding of aluminum to steel. J Manuf Sci Eng 2018;140:121002.
[22] Lee T, Zhang S, Vivek A, Daehn G, Kinsey B. Wave formation in impact welding: study of the Cu–Ti system. CIRP Ann 2019;68:261–4.
[23] Godunov S, Deribas A, Zabrodin A, Kozin N. Hydrodynamic effects in colliding solids. J Comput Phys 1970;5:517–39.
[24] Szecket A, Mayseless M. The triggering and controlling of stable interfacial conditions in explosive welding. Mater Sci Eng 1983;57:149–54.
[25] Date H, Kobayakawa S, Naka M. Microstructure and bonding strength of impact-welded aluminium–stainless steel joints. J Mater Process Technol 1999;85:166–70.
[26] Wang X, Wang X, Li F, Lu J, Liu H. Interface kinematics of laser impact welding of Ni and SS304 based on jet indentation mechanism. Metall Mater Trans A 2020;51A:2893–904.
[27] Wang H, Vivek A, Wang Y, Taber G, Daehn GS. Laser impact welding application in joining aluminum to titanium. J Laser Appl 2016;28:032002.
[28] Frank AM, Trottt WM. Investigation of thin laser-driven flyer plates using streak imaging and stop motion microphotography. In: American Institute of Physics Conference Proceedings. vol. 370. American Institute of Physics; 1996.
[29] Gleason G, Sunny S, Mathews R, Malik A. Numerical investigation of the transient interfacial material behavior during laser impact welding. Scr Mater 2022;208:114325.
[30] Nassiri A, Chini G, Vivek A, Daehn G, Kinsey B. Arbitrary Lagrangian–Eulerian finite element simulation and experimental investigation of wavy interfacial morphology during high velocity impact welding. Mater Des 2015;88:345–58.
[31] Sapanathan T, Raoelison RN, Padayodi E, Buiron N, Rachik M. Depiction of interfacial characteristic changes during impact welding using computational methods: comparison between arbitrary Lagrangian-Eulerian and Eulerian simulations. Mater Des 2016;102:303–12.
[32] Li Z, Wang X, Yang H, Ni P, Li F, Liu H. Numerical studies on laser impact welding: smooth particle hydrodynamics (sph), Eulerian, and sph-Lagrange. J Manuf Process 2021;68:43–56.
[33] Benson DJ. A mixture theory for contact in multi-material Eulerian formulations. Comput Methods Appl Mech Eng 1997;140(1–2):59–86.
[34] Fabbro R, Fournier J, Ballard P, Devaux D, Virmont J. Physical study of laser-produced plasma in confined geometry. J Appl Phys 1990;68:775–84.
[35] Hatamleh MI, Mahadevan J, Malik A, Qian D, Kovacevic R. Prediction of residual stress random fields for selective laser melted A357 aluminum alloy subjected to laser shock peening. J Manuf Sci Eng 2019;141:101011.
[36] Hong X, Wang S, Guo D, Wu H, Wang J, Dai Y, Xia X, Xie Y. Confining medium and absorptive overlay: their effects on a laser-induced shock wave. Opt Lasers Eng 1998;29:447–55.
[37] Menikoff R. Empirical equations of state for solids. In: ShockWave science and technology reference library. Springer; 2007. p. 143–88.
[38] Wang X, Li F, Huang T, Wang X, Liu H. Experimental and numerical study on the laser shock welding of aluminum to stainless steel. Opt Lasers Eng 2019;115:74–85.
[39] Isbell W, Shipman F, Jones A. Hugoniot equation of state measurements for eleven materials to five megabars. General Motors Technical Center, Warren, MI Materials and Structures Lab; 1968. Technical Report.
[40] Wang X, Shao M, Gao S, Gau J-T, Tang H, Jin H, et al. Numerical simulation of laser impact spot welding. J Manuf Process 2018;35:396–406.
[41] Harrison W, Loupias C, Outrebon P, Turland D. Experimental data and hydrocode calculations for hypervelocity impacts of stainless steel into aluminium in the 2–8 km/s range. Int J Impact Eng 1995;17:363–74.
[42] Committee AIH, et al. In: Metals handbook, vol. 2: properties and selection: nonferrous alloys and special-purpose materials. 3. ASM International; 1990. p. 5.